Journal of Materials Chemistry B

ROYAL SOCIETY OF CHEMISTRY

PAPER

View Article Online
View Journal | View Issue

Cite this: J. Mater. Chem. B, 2025, 13, 5808

Multifunctional PLGA nanocomposites to improve beta cell replacement therapy in Type 1 diabetes†

Cátia Vieira Rocha, Andreia Patrícia Magalhães, Victor Gonçalves, Lara Diego-González, Manuel Bañobre-López and Juan Gallo *

Received 21st January 2025,
Accepted 16th April 2025

DOI: 10.1039/d5tb00148j

rsc.li/materials-b

Diabetes Mellitus is a rapidly growing global health problem, with its prevalence having risen sharply in recent years. Type 1 diabetes (T1D) treatment options are limited, with most of them significantly compromising the quality of life of these patients. This study presents the development and characterization of a multifunctional hybrid nanoformulation (mHNFs) designed to enhance the efficacy of beta cell replacement therapy in T1D. By encapsulating rapamycin and two types of magnetic nanoparticles (MnO and Fe_3O_4) within PLGA, we aimed to address critical challenges in islet transplantation, including hypoxia and immunosuppression. The synthesized nanoparticles demonstrated dual imaging capabilities as MRI contrast agents, sustained drug release, and *in situ* oxygen generation, crucial for mitigating islet hypoxia and loss of function. *In vitro* studies confirmed the cytocompatibility of the system and its efficient internalization by rin-m cells. Additionally, O_2 generation studies proved that mHNFs significantly reduced hypoxia levels. These results highlight the potential of these nanocarriers to improve the safety and efficacy of T1D islet transplantation treatments through a multifunctional approach.

Introduction

Diabetes Mellitus is the fastest-growing health challenge worldwide, with the affected population having tripled in recent years.[1] In 2022, 8.75 million patients were living with type 1 diabetes (T1D).[2] Insulin therapy, administered through regular injections or continuous infusion, is the primary treatment for T1D to maintain normoglycemia. Transplantation is frequently used in T1D patients as a treatment to replace damaged insulin-producing cells (β-cells). This approach is particularly appropriate for patients experiencing severe hypoglycemic episodes and showing poor awareness of their blood sugar levels. Islet transplantation (IT) has emerged as a minimally invasive alternative to pancreas transplantation. In this procedure, islets of Langerhans from a donor pancreas are infused into the recipient's liver. This allows the body to produce insulin naturally, helping to maintain better glycemic control and external insulin independence. Unlike whole pancreas transplantation, IT preserves the recipient's own organ structure and function, reducing surgical risks and recovery time. IT offers the advantages of a less invasive procedure and steroid-free immunosuppression, which minimizes the side effects commonly associated with long-term steroid use. This allows for a more targeted approach to preventing organ rejection, while achieving outcomes comparable to those of pancreas transplantation.[3,4] However, several obstacles still hinder the widespread of this therapy, the main one being a decline in insulin independence from 50% in the first year after IT, to approximately 30% at 5 years,[5] most likely due to loss of islet function. Hypoxia-associated events have been quoted as the main responsible for the loss of islet function *peri*-transplantation,[6] since β-cells consume large amounts of oxygen during insulin secretion.[7] The life-long uncontrolled systemic immunosuppression and its associated side effects represent another of the drawbacks of this therapy.[5]

Novel nanotechnological approaches can be used for the simultaneous treatment and follow-up of IT, localizing the action of immunosuppressive drugs (limiting thus their side effects), while generating O_2 *in situ* to minimize hypoxic events and providing a non-invasive means for longitudinal follow-up of the treatment. Herein, we propose multifunctional nanoparticles (NPs) based on a biocompatible, biodegradable and FDA (U.S. Food and Drug Administration)/EMA (European Medicines Agency)-approved copolymer, poly(lactic-*co*-glycolic acid) – PLGA –[8,9] as theranostic (therapy plus diagnostic/monitoring) agents to improve the outcome of IT. PLGA is a widely used polymer in nanotechnology, allowing for the encapsulation of both organic and inorganic materials, such as small molecule drugs,[8,10,11] vaccines,[12] proteins,[13,14] metallic[15] and magnetic nanoparticles (MNPs).[16,17] Furthermore, the choice of PLGA stems, beyond its minimal toxicity, to its remarkable versatility,

Advanced Magnetic Theranostic Nanostructures Lab, International Iberian Nanotechnology Laboratory, Braga, Portugal. E-mail: juan.gallo@inl.int

† Electronic supplementary information (ESI) available. See DOI: https://doi.org/10.1039/d5tb00148j

since properties such as degradation rate, hydrophobicity and size can be tuned during the NP synthesis.[18]

Rapamycin (RPM), also known as sirolimus, is extensively used as an immunosuppressant and antiproliferative agent in transplantation as it inhibits the activation and proliferation of lymphocytes.[19,20] In its mechanism of action, rapamycin binds to a protein called FKBP12. This complex binds to and inhibits the mTOR pathway, resulting in a cell cycle arrest at the G1 phase contributing to the modulation, not only of lymphocytes but also other cells of the immune system, namely macrophages and dendritic cells.[21–23] However, the use of rapamycin can lead to serious side effects,[24] making encapsulation/controlled application crucial for a safe administration.

MNPs are used in various biomedical applications due to their biocompatibility and unique magnetic properties, characterized by a tailored response to an applied magnetic field. Additionally, selected MNPs display responsive behaviours to changes in pH and redox state. Within MNPs, MnO NPs are paramagnetic, thus do not retain magnetization in the absence of a magnetic field.[25,26] These NPs have been widely proposed for medical imaging as magnetic resonance imaging (MRI) T_1 contrast agents (CAs) (shortening the longitudinal relaxation time, T_1) and can also be used for O_2 generation through decomposition and/or oxidation processes.[11,27,28] Similarly, Fe_3O_4 NPs are extensively used in nanomedicine. These NPs offer unique properties since below a critical diameter (<15–20 nm) they showcase a superparamagnetic behaviour,[29] showing a relatively high saturation magnetization and null coercive forces or remanence. This property enables their use as theranostics *e.g.* combining therapy *via* magnetic hyperthermia with imaging *via* T_2-weighted MRI (shortening the transverse relaxation time, T_2, much more efficiently than MnO NPs). Their encapsulation in various nanocomposites, namely PLGA micro- and nanoparticles, has been studied to develop multifunctional composites for diagnostic and/or therapeutic purposes.[30] However, the potential of MNPs in immunosuppressive-theranostic applications has been largely overlooked so far.

In this context, we propose that by utilizing multifunctional magnetic hybrid nanocomposites, it is possible to minimize hypoxia, prevent immune rejection of islets while reducing side effects, and longitudinally monitor islet fate through MRI. The encapsulation of all the aforementioned components (Mn- and Fe-based MNPs, immunosuppressing drugs) into a polymeric drug delivery system contributes to (i) improve active principle solubility and protection against degradation, (ii) improve specificity and drug/O_2 release kinetics, and (iii) reduce off-target effects.[31] The envisioned methodology, illustrated in Fig. 1, involves treating isolated islets from the donor's pancreas with dual PLGA@MnO–Fe_3O_4@RPM (mHNF) to prevent hypoxia-induced β-cell death during *ex vivo* culture. Subsequently, treated islets will be infused into the recipient's portal vein and monitored longitudinally using MRI. Finally, mHNFs will be administered to the recipient to suppress immune rejection, mitigate hypoxia with encapsulated O_2-generating MnO NPs, and track the islets' fate through multimodal T_1–T_2 MRI imaging. This minimally invasive approach aims to enhance and sustain insulin independence for an extended period following IT by preserving islet function over time.

Materials and methods

Chemicals

Resomer® RG 752 H, poly(D,L-lactide-*co*-glycolide) copolymer, monomer ratio 75 : 25, M_w = 4000–15 000 Da, poly(vinyl alcohol) (PVA), M_w = 9000–10 000, 80% hydrolyzed, dichloromethane (DCM), acetonitrile HPLC grade (>99.93%), trifluoroacetic acid (TFA) HPLC grade (≥99%), phosphate-buffered saline (PBS), hydrogen peroxide solution (30% w/w), and tris(2,2′-bipyridyl)dichlororuthenium(II) hexahydrate were purchased from Merck KGaA (Darmstadt, Germany). Rapamycin (Sirolimus) was obtained from ADOOQ Bioscience (CA, USA). DiO′

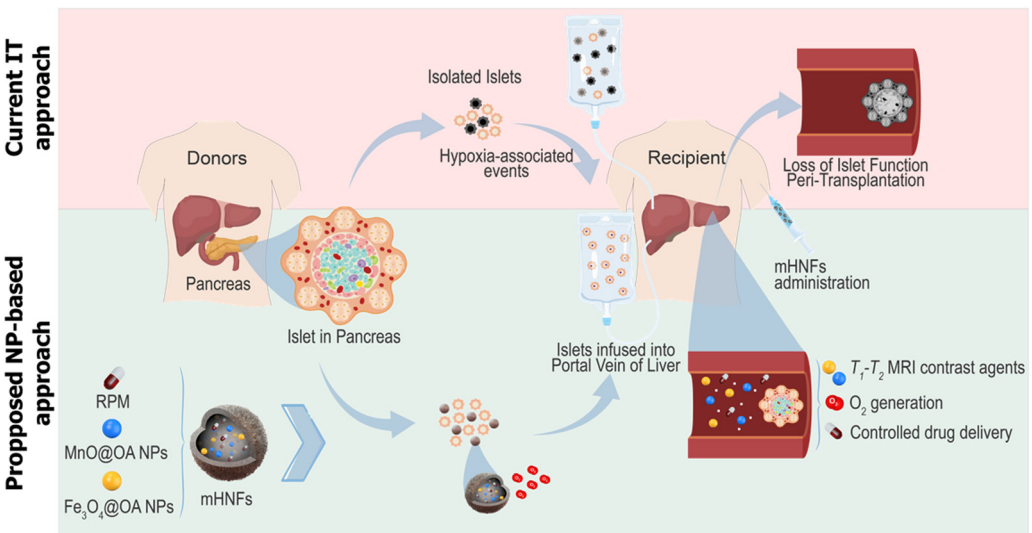

Fig. 1 Schematic representation of top, current IT procedure (red background), and bottom, proposed protocol using mHNFs (green background).

(3,3′-dioctadecyloxacarbocyanine Perchlorate) was purchased from ThermoFisher scientific (Dreieich, Germany).

Synthesis of MNPs

The synthesis of Fe_3O_4@OA NPs followed a previously established co-precipitation method by Almeida *et al.*[32] The synthesis of MnO@OA NPs was done *via* thermal decomposition of $MnOA_2$ as described in ref. 33. The characterization of these MNPs is presented in the support information.

Synthesis of magnetic immunosuppressive PLGA NPs (mHNFs)

PLGA NPs co-encapsulating RPM and MNPs (MnO and Fe_3O_4), were synthesized by an emulsification-solvent evaporation method – water-in-oil-in-water (WOW) emulsion (Fig. 2a).[34]

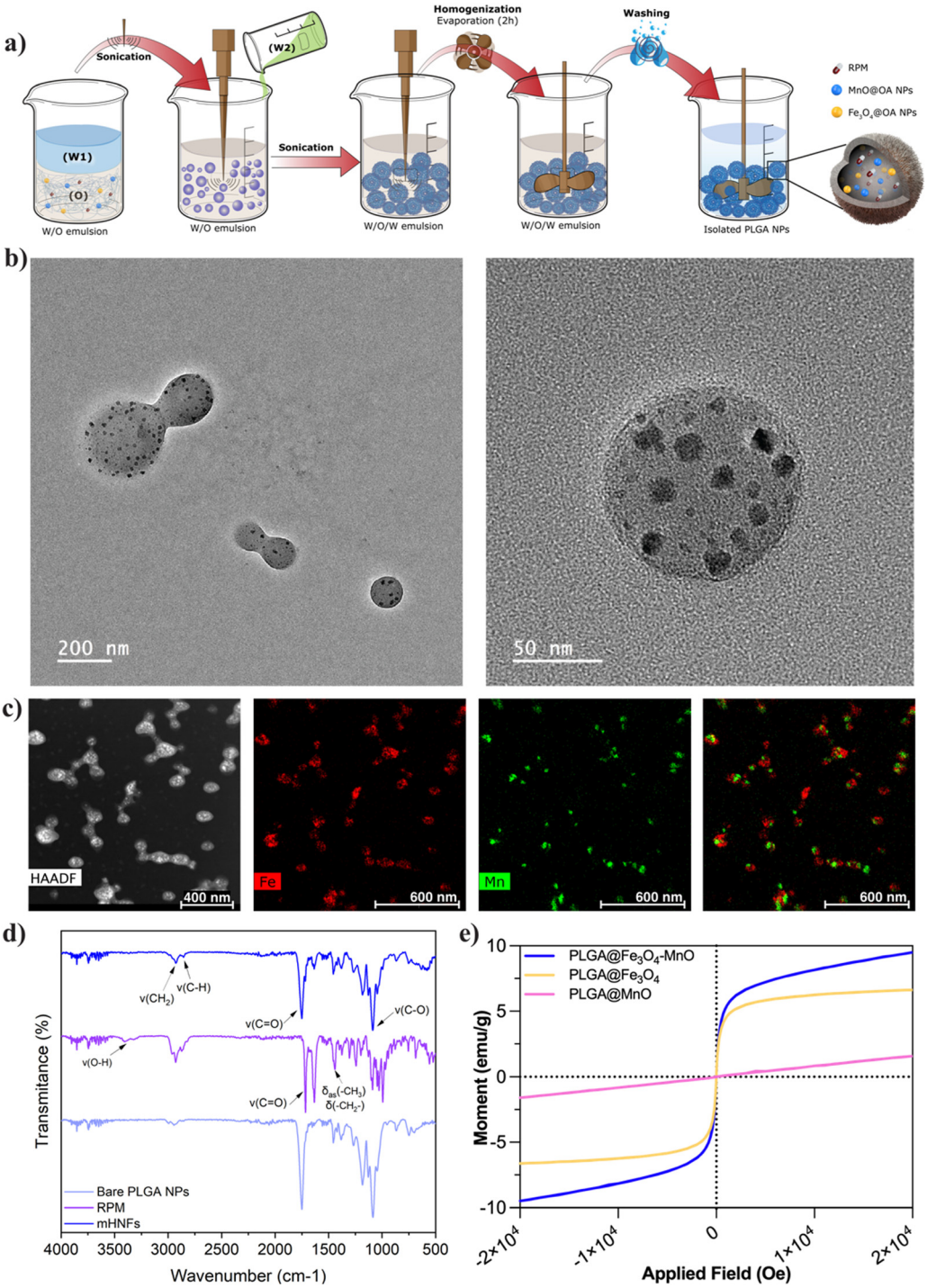

Fig. 2 (a) Schematic representation of emulsification-solvent evaporation synthesis (WOW emulsion); (b) TEM micrographs of the mHNFs at different magnifications, (c) HAADF image and STEM-EDX maps of the mHNFs for Fe, Mn and overimposed Fe plus Mn, (d) FTIR spectra and (e) magnetization curves as a function of applied field for mHNFs and controls.

Briefly, 20 mg of rapamycin, 300 μL of MnO (11 mg Mn per mL) and 30 μL of Fe_3O_4 (70 mg Fe per mL) NPs in chloroform were added to a 1,25 mL of a PLGA solution in DCM (100 mg mL^{-1}). This organic phase was emulsified by ultrasonication (90 s, 25% amplitude) with a first water phase of 125 μL (water-in-oil emulsion); a second water phase of 5 mL containing PVA as a stabilizer (20 mg mL^{-1}) was added to the previous emulsion and sonicated under the same conditions, obtaining a water-in-oil-in-water emulsion. Subsequently, the emulsion was diluted in 25 mL of Milli-Q and left to evaporate the organic solvent for 2 h. Finally, the NPs were purified by centrifugation (9000 rpm, 15 min). To maintain the original state of the synthesized NPs, they were freeze-dried with 1% of sucrose as cryoprotectant. For confocal microscopy studies 125 μL of a chloroform solution of DiO (1 mg mL^{-1}) was also added to the organic phase at the beginning of the synthesis.

Characterization of the mHNFs

Nanoparticle size, size distribution and zeta potential were determined by dynamic light scattering – DLS (SZ-100Z, Horiba Scientific). The analysis was performed at room temperature with a scattering angle of 90° and a NP dilution of 1 : 100. The morphology of the nanoformulation was examined by transmission electron microscopy – TEM (JEOL JEM-2100-HT) and the mapping of the encapsulated elements (Fe and Mn) was performed by STEM-EDX (FEI Titan ChemiSTEM). The concentration of each metallic element was determined using inductively coupled plasma atomic emission spectroscopy – ICP-AES (ICPE-9000, Shimadzu). The infrared spectra of the mHNFs were obtained using a Fourier transfer infrared – FTIR – instrument (Vertex 80v, Bruker). The mHNF were magnetically characterized using a vibrating-sample magnetometer – VSM (3473-70, GMW magnet systems).

Rapamycin encapsulation and release studies

To determine the encapsulation efficiency (EE%) of RPM, the total amount of encapsulated drug was calculated indirectly by measuring the non-encapsulated drug from the supernatants from NP purification through centrifugation. The non-encapsulated drug was quantified by reverse-phase high-performance liquid chromatography – RP-HPLC (1290 Infinity II LC System, Agilent). All separations were achieved using a C18, 15 cm × 0.21 cm, 5 μm column (TR-025078, Teknokroma) maintained at 70 °C. A gradient method (Table 1) was employed using acetonitrile:water with 0.1% of TFA as mobile phase at a flow rate of 0.5 mL min^{-1}. The UV detection wavelength was 278 nm.

Table 1 Gradient method employed to determine RPM concentration

Time (min)	Water (%)	Acetonitrile (%)
0	70	30
10	25	75
12	25	75
15	10	90
15, 1	70	30
18	70	30

To calculate the percentage of encapsulated drug, the following equation was employed:

$$EE\% = \frac{[\text{encapsulated drug}]}{[\text{total drug}]} \times 100$$

Drug release studies were performed using a pur-a-lyzer dialysis kit (6 kDa, Merck KGaA) with 0.6 mL of the nanoformulations, in 10 mL of PBS : ethanol buffer (9 : 1) at 37 °C, for two weeks. Release studies were performed under sink conditions, meaning that a volume of the host dissolution media was used to ensure the dissolution of at least 3 times the amount of drug in the dosage form. Aliquots (0.5 mL) were sampled at individual time intervals. Each aliquot was analyzed by HPLC as previously described, to determine the cumulative drug release profile of RPM.

O_2 generation studies

O_2 generation by the mHNFs was qualitatively defined by an optical method based on the quenching of the fluorescence intensity (FI) of a ruthenium probe (tris(2,2′-bipyridyl)dichlororuthenium(II) hexahydrate) by oxygen.[35] To evaluate oxygen generation, first, the ruthenium aqueous solution (5×10^{-5} mol L^{-1}, 1 mL) was bubbled with N_2 for 20 min to remove all dissolved O_2, before sealing with a rubber septum. Right before the measurement, a degassed (20 min, N_2) aqueous solution of mHNFs ([Mn] = 0.171 mg mL^{-1}) and 10 μL of H_2O_2 at a concentration of 50 mM were added to the ruthenium solution. The FI was measured every 15 min for 3 h. The sample was excited at λ_{ex} = 452 nm and its emission was measured at λ_{em} = 608 nm, by spectrofluorimetry (Fluoromax-4, Horiba Scientific). Two control tests were also performed: without the addition of H_2O_2 and replacing the aqueous solution with Milli-Q water.

Contrast generation studies

A MR solutions 3.0 T benchtop MRI system was used to evaluate the efficiency of prepared formulations as MRI contrast agents. The concentrations of Mn tested ranged from 0 to 300 μM, and the concentrations of Fe ranged from 0 to 150 μM. The relaxivity was calculated from the T_1 and T_2 maps, acquired using MPRAGE (magnetization prepared rapid gradient echo) and MEMS (multi-echo multi-slice) sequences respectively. The longitudinal (r_1) and transverse (r_2) relaxivity were calculated as the slope of the curve fitting $1/T_1$ (R_1) *versus* metal (Fe or Mn) concentration in mM. All MR images were acquired with an image matrix 256 × 252, FOV 60 × 60 mm, N_A = 15. The acquisition parameters used are listed in Table 2. Image J (Fiji) software was used to reconstruct the maps using the "MRI analysis calculator" plugin by Karl Schmidt.[36]

For the relaxometry measurements, T_1 and T_2 relaxation times were measured with a Minispec mq60 relaxometer (mq60, Bruker, B_0 = 1.41 T) operating at 60 MHz. At least four concentrations (0–2 mM) of Fe or Mn metals were measured. Saturation recovery (SR) and Carr–Purcell–Meiboom–Gil (CPMG) sequences were used to calculate the T_1 and T_2 relaxation times, respectively. The relaxivity was calculated as in the MRI experiments (Fig. S1, ESI†).

Table 2 Parameters used in the acquisition of MRI parametric maps

	Echoes	T_R (ms)	T_E (ms)	T_I (ms)	Slices	Slice thickness (mm)	A_T (min)
MPRAGE	11	10 000	5	50	1	2	50
MEMS	10	1400	15	15	3	1	32

In vitro studies

Human peripheral blood mononuclear cells (hPBMCs) were obtained from healthy donors by density gradient centrifugation (Ficoll, GE HealthCare, IL, USA) from whole blood. The hPBMCs were recovered, washed with PBS and kept in culture medium until their use in downstream experiments. The RIN-m cell line was acquired from the American Type Culture Collection (ATCC). The culture medium used in both cases was Roswell Park Memorial Institute medium – RPMI (Merck KGaA) supplemented with 10% inactivated fetal bovine serum – FBS (Merck KGaA) and 1% of penicillin/streptomycin (Gibco™, Thermo Fisher Scientific), at 37 °C in 5% CO_2 atmosphere. In the case of RIN-m cells, their maintenance was performed every three – four days, when the cell confluence reached 70–80%.

Cell viability and toxicity assays. The fluorometric AquaBluer reagent (MultiTarget Pharmaceuticals LLC) was used to determine changes in cell viability after 48 h of incubation with the different nanoformulations at concentrations of RPM of 0.1, 1, 10, 25, and 50 μg mL^{-1}.

PBMCs and RIN-m cells were seeded on 96-flat well plates at a density of 5×10^4 and 1×10^4 cells per well, respectively. Next day, the NPs treatments were added and incubated for 48 h at 37 °C and 5% CO_2. Culture medium alone and with samples was used as background to discard any potential interference of the drug and NPs in the measurements. After the incubation time, the AquaBluer reagent at a 1 : 100 dilution in culture medium was added and incubated for 4 h according to the manufacturer's instructions. Finally, the FI was measured (λ_{ex} = 540 nm, λ_{em} = 590 nm) in a microplate reader (SYNERGY H1, Biotek). The percentage of cell viability was calculated following the formula below:

$$\text{Cell viability (\%)} = \frac{\text{FI(Cells + Drug)} - \text{FI(Drug)}}{\text{FI(Cells - Culture medium)}} \times 100$$

Internalization studies. Confocal microscopy was used to study the internalization of PLGA nanoparticles in RIN-m cells. Cells were treated with the PLGA NPs and incubated for 24 h, at a clinically relevant concentration of metals of 17.4 μg mL^{-1}. Afterwards, the cells were washed with PBS, fixed in 4% PFA (15 min at RT) for 10 min at 4 °C. Cortical actin was stained with 50 μg mL^{-1} phalloidin-TRITC for 1 h at 4 °C. Finally, cells were washed with PBS and the nuclei counterstained with DAPI (ProLong™ Gold Antifade Mountant with DNA Stain DAPI, Thermofisher). Images were acquired using a Zeiss LSM780 confocal laser scanning microscope (Oberkochen, Germany) equipped with 405 nm and 561 nm diode lasers and a 488 nm argon laser, and analyzed using the Zen 2010 software and Fiji.

MRI contrast generation studies. To study the ability of the NPs to generate contrast in cells, RIN-m cells were seeded in 96-flat well plates at a density of 1.5×10^4 cells per well and were treated with a control PLGA@MnO at 50 and 100 μg mL^{-1} of Mn, and mHNFs at 2 and 3 μg mL^{-1} (corresponding to 25 μg mL^{-1} of RPM) of Mn for 48 h. Following incubation, the cells were washed with PBS, pooled, and transferred to Eppendorf tubes. The samples were then centrifuged at 13 400 rpm for 5 min, to collect the cell pellets, which were subsequently used for MRI acquisition. The relaxivity was extrapolated from the T_1 and T_2 maps, acquired using MEMS and FLASH (fast low-angle shot) sequences with the following parameters: image matrix 256 × 128; FOV 60 × 60 mm; echoes = 128; slices = 1; A_T = 4.52 min; T_R = 10 ms; T_E = 4 ms; T_I = 50–5130 ms. Image J (Fiji) and Preclinical scan™ software were used to reconstruct the maps like previous MRI studies.

Hypoxia remediation studies. The ability of the mHNFs to generate oxygen and reduce hypoxia in β-cells was determined using the Image-iT Green Hypoxia Reagent (Invitrogen, ThermoFisher Scientific). Briefly, RIN-m cells were seeded in 96-flat well plates at a density of 1×10^4 cells per well and incubated for 48 h at 37 °C with 5% CO_2. Next, the medium was removed and replaced with fresh growth medium containing the Image-iT™ Green Hypoxia Reagent at a final concentration of 10 μM, and cells were incubated for 1 h. Afterward, cells were treated with control PLGA@MnO NPs at concentrations of 50 and 100 μg mL^{-1} and mHNFs at concentrations of Mn of 3 and 6 μg mL^{-1}, corresponding to drug concentrations of 25 and 50 μg mL^{-1}. Hypoxia conditions were achieved using Compact W-Zip Seal Pouches (Oxoid™, Thermo Scientific™) with CampyGen™ Compact Sachets (Oxoid™, Thermo Scientific™) for 24 h. The hypoxic atmosphere was confirmed by the color change of the Resazurin Anaerobic Indicator (Oxoid™, Thermo Scientific™), which was added alongside the sachet. Post hypoxic exposure, cells were washed twice with PBS and stained with DAPI (ProLong™ Gold Antifade Mountant with DNA Stain DAPI, Thermofisher). Fluorescence intensity was measured (λ_{ex} = 488 nm, λ_{em} = 520 nm) using a microplate reader (SYNERGY H1, Biotek) and fluorescent images were captured in a Zeiss LSM780 confocal laser scanning microscope (Oberkochen, Germany). Images were analyzed using the Zen 2010 software and Fiji.

Results and discussion

Synthesis and physico-chemical characterization

A double emulsion (water in oil in water, WOW) synthesis protocol was selected for the preparation of the formulations due to its simplicity and versatility that allows for the encapsulation of both hydrophilic and hydrophobic compounds.[30] The low molecular weight of the chosen PLGA facilitates the formation of smaller particles and enhances the encapsulation

efficiency of small molecules, due to the reduced chain length of the polymer.[8,37] Since a lower molecular weight can also enhance the degradation rate of the polymer, a monomer ratio of 75 : 25 (lactic acid : glycolic acid) was specifically chosen to balance this property. Lactic acid is more hydrophobic making it more difficult for water to penetrate the polymer matrix, thereby slowing down the hydrolysis process. This leads to a slower degradation rate which is crucial to achieving a controlled and sustained release of the drug.[8,30]

Fe_3O_4@OA NPs and MnO@OA NPs with average sizes of 9.7 ± 1 nm and 12.2 ± 2 nm, respectively (>300 NPs measured from TEM micrographs) were encapsulated into PLGA NPs. In this study we worked with four different nanoformulations; the final mHNFs incorporating both the drug and Fe/Mn MNPs, and three control formulations: PLGA@Fe_3O_4, PLGA@MnO and PLGA@RPM to better understand the behaviour of the mHNFs. The double emulsion WOW synthesis used (Fig. 2a) proved very reproducible, with all the formulations presenting similar size and morphology regardless of the nature of the loading. ICP analysis revealed the concentration of each magnetic component in the final formulation: [Fe] = 0.3 μg mL^{-1} and [Mn] = 0.2 μg mL^{-1}. DLS analysis of as prepared final NPs revealed an average hydrodynamic diameter of 218 ± 3 nm, with a polydispersity index of 0.11 ± 0.06 and a negative zeta-potential of −43 ± 2 mV. These values suggest that the particles are well-suited for systemic administration and will exhibit excellent stability in solution. TEM was also used to determine the size of the particles by measuring individual NPs (n = 140), obtaining a value of 137 ± 39 nm.[37] As expected, this value is smaller than the one obtained by DLS, due to the drying process in TEM sample preparation and the fact that DLS provides the hydrodynamic diameter, size of the particles plus the water moving with them. TEM images (Fig. 2b) showed that the nanoparticles present a spherical form and efficiently encapsulate the MNPs, clearly visible as hypointense, much smaller, pseudo-spherical nanoparticles. Through STEM-EDX mapping (Fig. 2c) it was possible to confirm the simultaneous presence of both Fe_3O_4 and MnO inside a single PLGA NP matrix.

Fig. 2d displays all the relevant FTIR spectra to characterize the final mHNFs. The characteristic bands at 2998 and 2954 cm^{-1} are attributed to the C–H stretching vibrations from the polymer. At approximately 1700 cm^{-1}, the carbonyl group stretching of the PLGA polymer is well pronounced, and at 1300–1000 cm^{-1} the stretching of C–O is also noticeable. RPM absorption bands overlap these wavelengths, making it difficult to conclude the presence of the drug in the mHNFs from them. However, the mHNFs spectrum shows a peak at 1500 cm^{-1}, the peak for the asymmetric and symmetric bending C–H vibration in RPM. A broad peak in the region 600–520 cm^{-1} is also visible coming from the stretching vibration of the Fe–O and Mn–O bonds from the MNPs. Overall, the chemical characteristics of the polymer dominate the FTIR spectra of the final mHNFs due to their much larger concentration and outward placement when compared to the drug and NPs.

The magnetic properties of the mHNFs and controls were studied by VSM. Fig. 2e shows the magnetization *vs.* applied field curves. As expected, PLGA@MnO NPs display a clear paramagnetic behaviour where the magnetization increases linearly with the applied field, whereas PLGA@Fe_3O_4 NPs show a superparamagnetic behaviour with zero coercive force or remanence and with a $M_s \approx 7$ emu g^{-1} (calculated after subtracting the PM signal). As predicted, the mHNFs exhibit overimposed superparamagnetic and paramagnetic behaviours, due to the presence of both paramagnetic MnO and superparamagnetic Fe_3O_4 NPs.

Functional characterization

Oxygen generation. One of the aims of this study was to develop a formulation able to release O_2 *in situ* to mitigate hypoxia conditions. Manganese oxide NPs proved efficient in the generation of O_2 in the presence of biologically relevant redox active species (*e.g.* H_2O_2).[38,39] To demonstrate this effect in mNHFs, an O_2-sensitive ruthenium-based probe ($Ru(bpy)_3$) (tris(bipyridine)ruthenium(II) chloride) was used. Fig. 3a shows the normalized fluorescence intensity (FI) of the probe and controls as a function of time in the presence and absence of H_2O_2. The FI of control samples (no MnO NPs or no H_2O_2) remained constant over a 3 h observation period. In contrast, the mHNFs exhibited a statistically significant decline in FI from the 45-minute mark onward when H_2O_2 is present. While MnO_2 is the material most commonly reported for O_2 generation, this experiment confirms that MnO also possesses the capability to generate O_2 in the presence of redox-active species. This specific generation of O_2 by mHNFs in the presence of redox active species, supporting our initial hypothesis.

Contrast generation. Other of the goals of this study was to deliver a formulation with imaging capacity to longitudinally and non-invasively follow the fate of the transplanted β-cells through MRI. The presence of MnO and Fe_3O_4 NPs within the mHNFs, should grant the system the required magnetic properties (Fig. 2d) to potentially function as both T_1 and T_2 contrast agents. To better understand the imaging behaviour of these samples, T_1 and T_2 relaxometry measurements and parametric T_1 and T_2 maps (Fig. 3b) were acquired at clinical fields of 1.5 T and 3.0 T. The parametric maps were used to calculate the relaxivity values (r_x) of the final mHNFs, which indicate how efficient the nanoparticles are as MRI CAs. For simplicity, only either Mn or Fe concentrations were considered to calculate r_1 and r_2, respectively.[11,40] r_1 and r_2 values of the mHNFs were 2.7 and 315 mM^{-1} s^{-1}, respectively at 1.5 T, and changed to 3.3 and 251 mM^{-1} s^{-1} when increasing the field strength to 3.0 T. This increase in r_1 is contrary to the expected behavior, as r_1 typically decreases with increasing field strength, due to changes in the mechanisms of energy transfer and spin interactions, which become less efficient as the field strength increases. This anomaly might be explained by an interaction between T_1 and T_2 relaxation processes, where the contribution of T_2 relaxation could influence the r_1 values, particularly in systems where the relaxation mechanisms are more complex.[41] Compared to commercially available CAs such as Teslascan®, a manganese-based CA (r_1 = 1.6 mM^{-1} s^{-1} at 1.5 T; r_1 = 1.5 mM^{-1} s^{-1} at 3.0 T) and Feridex®, an iron-based CA (r_2 = 41 mM^{-1} s^{-1} at 1.5 T; r_2 = 93 mM^{-1} s^{-1} at 3.0 T), the values

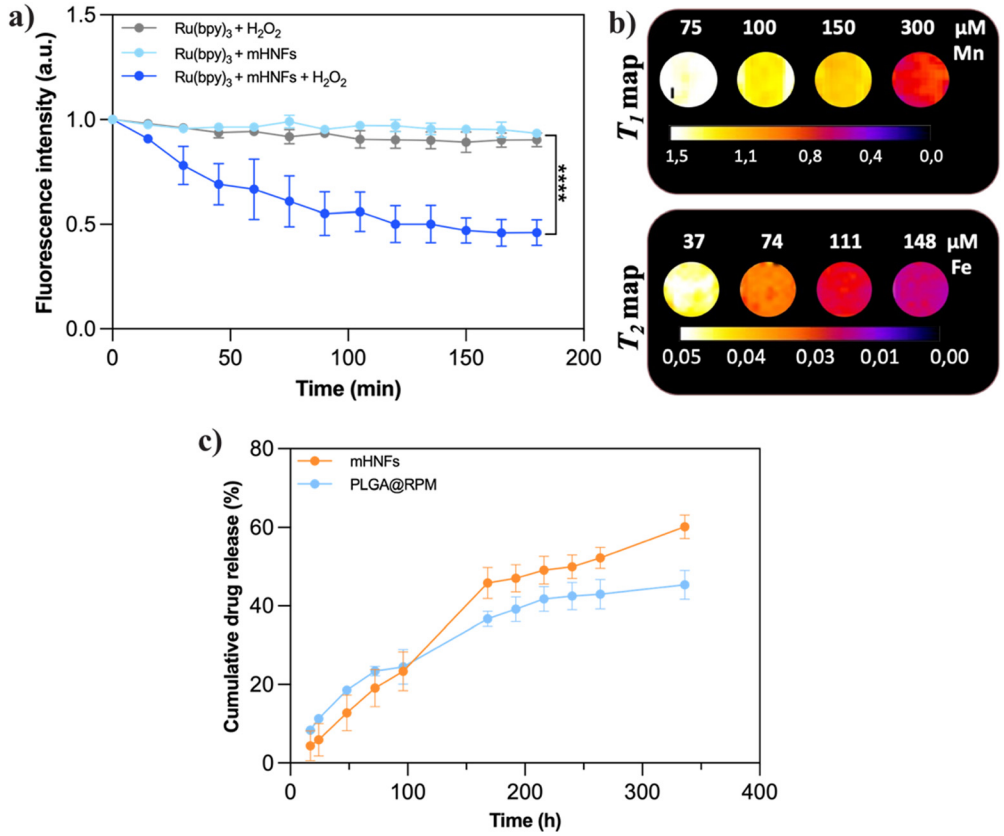

Fig. 3 (a) Fluorescence intensity of $Ru(bpy)_3$ probe over a 3 h period after the addition of mHNFs plus H_2O_2, and controls (grey – probe plus oxidizing agent; light blue – probe plus mHNFs; dark blue – probe plus mHNFs plus oxidizing agent); (b) pseudo-colored MRI parametric maps of mHNFs water dispersions at different concentrations; top: T_1 map, bottom, T_2 map. (c) Drug release profile for mHNFs (orange) and control formulation only without MNPs (blue).

obtained for mHNFs are remarkably higher at either field strength.[42] Translating these numbers into MR images, as can be seen in Fig. 3b, the different concentrations of mHNFs succeeded in creating a clear change in contrast in both modalities. This MR imaging performance confirms mHNFs as efficient dual T_1–T_2 MRI contrast agents under clinical field settings.

Encapsulation efficiency and drug release studies. The encapsulation efficiency of RPM in the final mHNFs as well as in the control formulations (PLGA, Fe_3O_4–PLGA and MnO–PLGA) was above 85% in all cases. No significant differences in EE% were observed between formulations (control without MNPs, 88 ± 2%; control with Fe_3O_4 only, 89 ± 1%; control with MnO only 91 ± 1%; mHNFs, 85 ± 8%). These results demonstrate that PLGA nano-matrices can efficiently encapsulate RPM with and without co-encapsulation of MNPs.

Drug release studies were then performed on the formulations for over 15 days. For the final mHNFs, 60% of the drug was released over 15 days, indicating that these nanocomposites are a promising drug delivery system for the sustained release of RPM. Control NPs of PLGA@RPM presented a similar drug release profile, with no significant differences compared to mHNFs. The sustained and controlled release of RPM for extended periods is beneficial to reduce side effects and allows for more precise dosage control, potentially leading to enhanced therapeutic outcomes. On top of that, a sustained release would benefit the patient by reducing the number of administrations required. To gain a deeper understanding of the drug release mechanism, the release data were fitted to various mathematical models (Table 3 and Table S1, ESI†). The Korsemeyer–Peppas model was the one providing the best fit. From this model the value of 'n' was calculated to be $n = 0.8 \pm 0.2$, indicating that the release of the drug follows an anomalous or non-Fickian diffusion ($0.5 > n > 1$). In this case, the mechanism of drug release is governed by diffusion and

Table 3 Values obtained from the fitting of the drug release data, to different mathematical models

Zero order			Higuchi			Korsmeyer–Peppas			
K_0	AIC	R^2	K_H	AIC	R^2	K_m	n	AIC	R^2
0.210 ± 0.027	67.52	0.882	3.120 ± 0.468	67.52	0.882	1.175 ± 1.276	0.765 ± 0.191	58.79	0.960

swelling. For the control NP-free formulation, PLGA@RPM, the fitting results are consistent with the ones of mHNFs. Overall, the co-encapsulation of MNPs and RPM does not alter the EE or the release profile of the drug, further demonstrating the versatility and robustness of PLGA nanoparticles as encapsulating and controlled drug delivery systems.

In vitro validation

Once the mHNFs were fully characterized, their theranostic properties were evaluated *in vitro*. Two different models were used for this purpose due to the different cellular targets of the different components of the nanoformulation: β-cells from rat (RIN-m cell line, ATCC CRL-2057) and primary PBMCs isolated from healthy human donor blood.

Cytotoxicity. The final mHNFs were evaluated together with control nanoformulations containing MNPs without the drug to better understand potential unexpected effects. First, the compatibility of the vehicle (and controls) was evaluated in β-cells and PBMCs. The range of metal concentrations tested (5 to 100 μg mL^{-1}) were expanded well beyond the concentrations used later for theranostic purposes to define toxicity limits. No significant toxicity was observed for any of the vehicle controls below 17.4 μg mL^{-1}. Above this concentration, the presence of MnO NPs induced a moderate dose-dependent decrease in viability. This effect has been previously observed in Mn-containing probes.[43] Although the decrease in viability for PLGA@Fe_3O_4–MnO NPs is not statistically significant, a downward trend was observed in both cell lines. Interestingly, this trend suggests that the combination of Fe and Mn could be slightly more toxic than either element alone, even though the effect is not statistically significant. One hypothesis for this trend would be that the combination of the two MNPs has a synergistic effect that exacerbates the oxidative stress in cells. This combined effect might push cellular stress beyond the threshold that either Fe or Mn alone would achieve, inducing apoptosis. This effect has been previously reported in cerebral models.[44] Nevertheless, as mentioned above, such high concentrations of Mn are not required to observe a therapeutic/theranostic effect (see below and Fig. 4c and d) and thus the formulations can be considered safe.

Next, to evaluate the therapeutic effect of the drug and the impact of its encapsulation, the cytotoxic effect of free RPM was compared to that of encapsulated RPM. For PBMCs, free RPM maintained stable viability across all concentrations up to the highest concentration tested (50 μg mL^{-1}), where viability abruptly dropped to 0%. Meanwhile, the nanoformulations showed a more progressive activity, starting to induce cell death already at 25 μg mL^{-1}. In the case of the RIN-m cell line, free RPM showed a similar profile to the one obtained for PBMCs, although in this case, the toxicity was already significant at 25 μg mL^{-1}. For this cell line, the encapsulated drug showed no decrease in viability up until the highest concentration (50 μg mL^{-1}), where there was a substantial decline. Encapsulation of RPM within PLGA NPs managed to reduce its toxicity

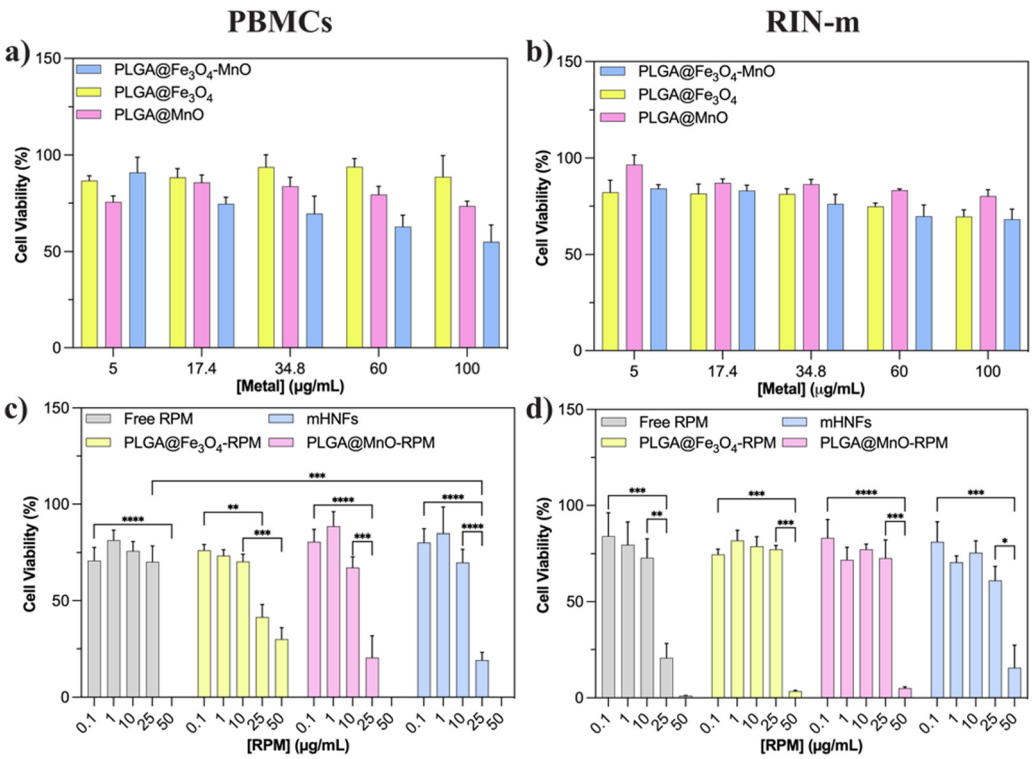

Fig. 4 Cell viability of control formulations for PBMCs (a), and RIN-m cell line (b); cell viability of formulations with rapamycin for PBMCs (c) and RIN-m (d). The data represents the mean value of SEM with a minimum of three independent experiments (*$p < 0.05$, **$p < 0.005$, ***$p < 0.0005$, ****$p < 0.0001$).

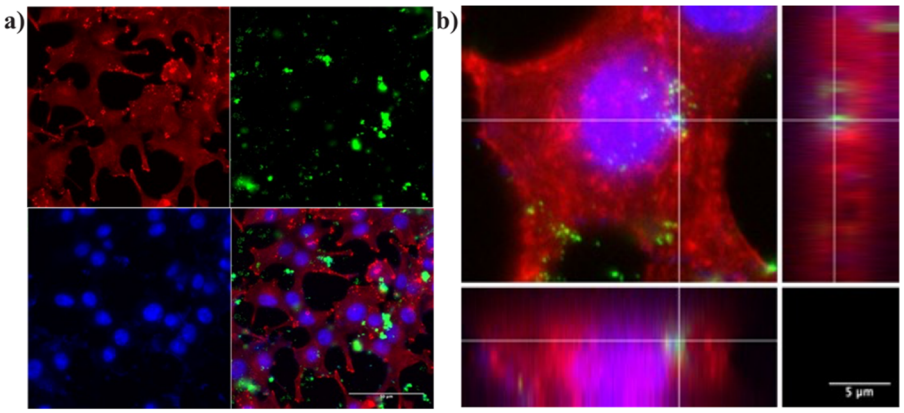

Fig. 5 Confocal projection images of RIN-m cells exposed to mHNFs during 24 h (a); confocal projection images of internalized mHNFs (b).

significantly in all versions of the formulation tested, further supporting the positive role of drug encapsulation. Overall, RPM encapsulation provides enhanced control over PBMCs viability while offering greater biocompatibility to insulin-producing cells compared to free RPM, making it a promising approach for improving therapeutic outcomes in T1D treatments.

Cell internalization. To assess the internalization of the mHNF nanoparticles, RIN-m cells were treated with mHNFs at a concentration of 17.4 μg mL^{-1} (based on metal content) for 24 h. NP cell internalization studies are crucial for understanding how nanoparticles interact with cells, which ultimately helps assess their safety and efficacy. Fig. 5 presents representative confocal microscopy images of RIN-m cells, with nuclei stained blue (DAPI) and cytoplasm stained red (α-tubulin). The fluorescence of mHNFs appears green due to the presence of DiO ($\lambda_{ex/em}$ = 489/506 nm) in the formulation. Although some nanoparticle aggregates (probably formed during to the lyophilization process[45]) are visible outside the cells, the majority of the nanoparticles are located within the cell cytoplasm, confirming their efficient internalization.

***In vitro* MRI.** Next, to evaluate the ability of the NPs to generate contrast in cells, RIN-m cells were seeded and treated with the mHNFs for 24 h and then collected to be analyzed by MRI. Fig. 6a shows the contrast generated in cells incubated with mHNFs compared to non-treated controls. The mHNFs nanoformulation presented a strong T_2 contrast generation of 184 ms *versus* the water control (T_2 = 936 ms). However, the T_1 effect was not so pronounced with a value of 2291 ms, closer to

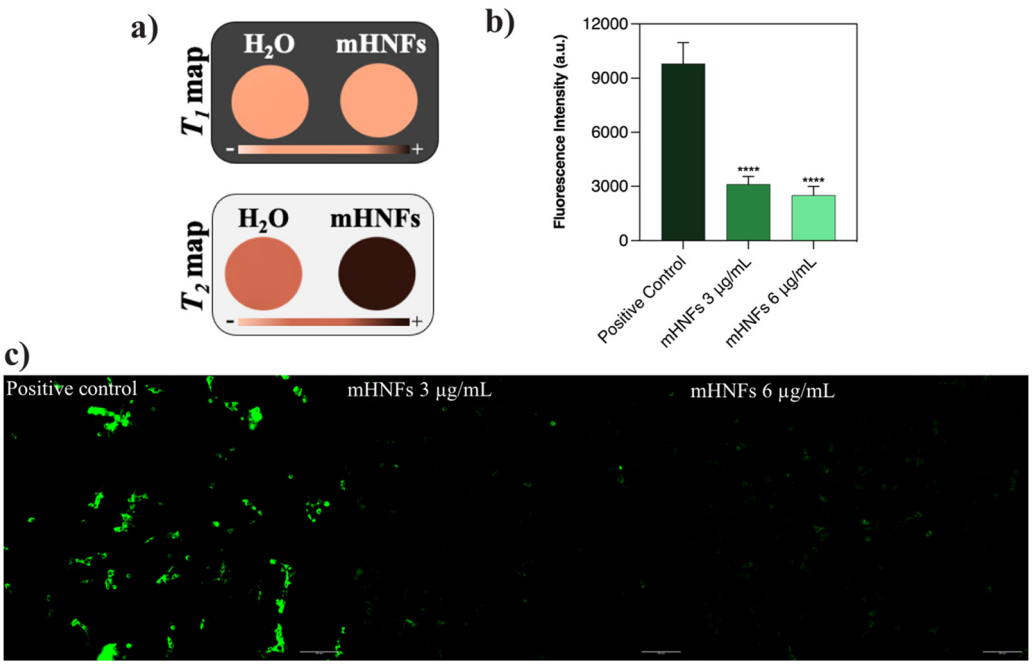

Fig. 6 (a) MRI parametric maps of mHNFs; top: T_1 map, bottom, T_2 map; (b) fluorescence intensity graph of Image-iT Green Hypoxia Reagent in RIN-m cells treated with mHNFs at different metal and drug concentrations, (c) corresponding fluorescence microscopy images. The data represents the mean value of SEM with a minimum of three independent experiments (****$p < 0.0001$).

the water control (T_1 = 2387 ms), but still statistically significant. This indicates that the concentration of Mn is either too low or the Fe is shielding the effect of Mn due to its higher concentration. The strong T_2 contrast achieved by mHNFs suggests that the combination of Mn and Fe, even at lower concentrations, is highly effective in enhancing MRI signals. Although the T_1 contrast for mHNFs is weaker, it remains noticeable, indicating that the formulation is still capable of performing as a dual T_1–T_2 MRI enhancer and generate contrast across both imaging modalities.

Hypoxia. The ability of the nanoformulations to generate O_2 demonstrated in solution was then tested *in vitro* in β-cells. Fig. 6b shows the FI of the IT green hypoxia reagent in RIN-m cells cultivated under hypoxia conditions and treated with mHNFs at concentrations of Mn of 6 and 3 μg mL^{-1}, corresponding to 50 and 25 μg mL^{-1} of RPM. A significant reduction in FI was observed in both cases, with a concentration dependent effect. This marked decrease in fluorescence was also supported by fluorescence microscopy (Fig. 6c), where cells treated with mHNFs display minimal green fluorescence, in contrast to the positive untreated control, which shows widespread green fluorescence. mHNF can effectively reduce hypoxia at therapeutically relevant drug concentrations. As in the in-solution experiments, it can be concluded that the MnO NPs within mHNFs react with endogenous redox active molecules to produce O_2 *in vitro*. This oxidative reaction happens as hypoxia induces oxidative stress in cells, leading to the overproduction of ROS (like H_2O_2). Additionally, this formulation offers a balanced approach by providing substantial hypoxia reduction along with immunomodulatory benefits, while potentially minimizing toxicity associated with its components.

Conclusion

This study successfully prepared, characterized and validated rapamycin-loaded magnetic PLGA nanocarriers for β-cell replacement therapy in T1D. The nanoformulation was suitable for systemic administration and displayed an overimposed superparamagnetic and paramagnetic behaviour, ideal for the intended dual-imaging purpose. The mHNFs exhibited longitudinal and transversal contrast in MRI, even when internalized into RIN-m cells. On the therapy side, the particles were able to generate O_2 due to the presence of manganese oxide, which translated into a mitigation of hypoxia *in vitro* even at low Mn concentrations. This will help prevent islet hypoxia *peri*-transplantation and avoid loss of function over time. The nanocarriers, engineered to encapsulate and sustain the release of rapamycin, proved successful, allowing for a prolonged and controlled release of the drug. The encapsulation was proved to be key to control PBMCs toxicity while preserving insulin-producing cells. This balance is crucial for maintaining therapeutic levels of immunosuppression, thus protecting transplanted islets from immune attack while reducing systemic toxicity. The particles did not present relevant toxicities in donor PBMCs and β-cells from rat within the active concentration range. The multifunctional properties of this nanocomposite highlight their potential to improve the current state of IT procedures, offering significant promise for enhancing the efficacy of transplantation therapies.

Authors' contributions

CVR wrote the manuscript, synthesized Fe_3O_4, prepared the final mHNFs, physico-chemically characterized them and validated them *in vitro*. APM and LDG performed *in vitro* studies. VG synthesized MnO@OA NPs and designed the ToC. MBL reviewed the manuscript. JG coordinated experiments and reviewed the manuscript.

Data availability

The authors declare that all data generated or analyzed during this study are included in this published article and its ESI.†

Conflicts of interest

There are no conflicts to declare.

Acknowledgements

This work was partially conducted using the INL User Facilities. This work was funded by the Fundação para a Ciência e a Tecnologia (FCT) through the grant UnTAM, PTDC/QUI-OUT/3143/2021. This study was also financed by project IBEROS+ (0072_IBEROS_MAIS_1_E, Interreg-POCTEP 2021-2027). CVR and VG would like to gratefully acknowledge the FCT for the doctoral grants 2020.08240.BD and 2020.10155.BD.

References

1 E. J. Boyko, D. J. Magliano, S. Karuranga, L. Piemonte, P. Riley, P. Saeedi and H. Sun, *International Diabetes Federation, IDF DIABETES ATLAS*, 10th edn, 2021, p. 141.
2 F. Wang, G. Ogle, G. Gregory and J. Maniam, *IDF ATLAS reports 2022*, 2022, p. 15.
3 R. Bottino, M. F. Knoll, C. A. Knoll, S. Bertera and M. M. Trucco, The future of islet transplantation is now, *Front. Med.*, 2018, **5**(202), 1–13.
4 B. Voglová, M. Zahradnická, P. Girman, J. Kríž, Z. Berková and T. Koblas, *et al.*, Benefits of islet transplantation as an alternative to pancreas transplantation: retrospective study of more than 10 ten years of experience in a single center, *Rev. Diabet Stud.*, 2017, **14**(1), 10–21.
5 B. Opałka, M. Żołnierczuk and M. Grabowska, Immunosuppressive Agents—Effects on the Cardiovascular System and Selected Metabolic Aspects: A Review, *J. Clin. Med.*, 2023, **12**(21), 6935.
6 H. Komatsu, F. Kandeel and Y. Mullen, Impact of Oxygen on Pancreatic Islet Survival, *Pancreas*, 2018, **47**, 533–543.

7 S. Keshtkar, M. Kaviani, Z. Jabbarpour, B. Geramizadeh, E. Motevaseli and S. Nikeghbalian, *et al.*, Protective effect of nobiletin on isolated human islets survival and function against hypoxia and oxidative stress-induced apoptosis, *Sci. Rep.*, 2019, **9**(11701), 1–13.
8 H. K. Makadia and S. J. Siegel, Poly Lactic-*co*-Glycolic Acid (PLGA) as biodegradable controlled drug delivery carrier, *Polymers*, 2011, **3**(3), 1377–1397.
9 F. S. T. Mirakabad, K. Nejati-Koshki, A. Akbarzadeh, M. R. Yamchi, M. Milani and N. Zarghami, *et al.*, PLGA-based nanoparticles as cancer drug delivery systems, *Asian Pac. J. Cancer Prev.*, 2014, **15**(2), 517–535.
10 Y. Choi, J. R. Joo, A. Hong and J. S. Park, Development of drug-loaded PLGA microparticles with different release patterns for prolonged drug delivery, *Bull. Korean Chem. Soc.*, 2011, **32**(3), 867–872.
11 C. Vieira Rocha, M. Costa da Silva, M. Bañobre-López and J. Gallo, (Para)magnetic hybrid nanocomposites for dual MRI detection and treatment of solid tumours, *Chem. Commun.*, 2020, **56**, 8695.
12 G. Cappellano, C. Comi, A. Chiocchetti and U. Dianzani, Exploiting PLGA-based biocompatible nanoparticles for next-generation tolerogenic vaccines against autoimmune disease, *Int. J. Mol. Sci.*, 2019, **20**(1), 204.
13 J. D. Ospina-Villa, C. Gómez-Hoyos, R. Zuluaga-Gallego and O. Triana-Chávez, Encapsulation of proteins from Leishmania panamensis into PLGA particles by a single emulsion-solvent evaporation method, *J. Microbiol. Methods*, 2019, **162**, 1–7.
14 C. B. Roces, D. Christensen and Y. Perrie, Translating the fabrication of protein-loaded poly(lactic-*co*-glycolic acid) nanoparticles from bench to scale-independent production using microfluidics, *Drug Delivery Transl. Res.*, 2020, **10**(3), 582–593.
15 E. N. Zare, R. Jamaledin, P. Naserzadeh, E. Afjeh-Dana, B. Ashtari and M. Hosseinzadeh, *et al.*, Metal-Based Nanostructures/PLGA Nanocomposites: Antimicrobial Activity, Cytotoxicity, and Their Biomedical Applications, *ACS Appl. Mater. Interfaces*, 2019, **12**(3), 3279–3300.
16 J. Ghitman, E. I. Biru, R. Stan and H. Iovu, Review of hybrid PLGA nanoparticles: future of smart drug delivery and theranostics medicine, *Mater. Des.*, 2020, **193**, 108805.
17 C. Liang, N. Li, Z. Cai, R. Liang, X. Zheng and L. Deng, *et al.*, Co-encapsulation of magnetic Fe_3O_4 nanoparticles and doxorubicin into biocompatible PLGA–PEG nanocarriers for early detection and treatment of tumours, *Artif. Cells, Nanomed., Biotechnol.*, 2019, **47**(1), 4211–4221.
18 S. Rezvantalab, N. I. Drude, M. K. Moraveji, N. Güvener, E. K. Koons and Y. Shi, *et al.*, PLGA-based nanoparticles in cancer treatment, *Front. Pharmacol.*, 2018, **9**(1260), 1–19.
19 R. N. Saunders, M. S. Metcalfe and M. L. Nicholson, Rapamycin in transplantation: a review of the evidence, *Kidney Int.*, 2001, **59**(1), 3–16.
20 A. Haddadi, P. Elamanchili, A. Lavasanifar, S. Das, J. Shapiro and J. Samuel, Delivery of rapamycin by PLGA nanoparticles enhances its suppressive activity on dendritic cells, *J. Biomed. Mater. Res., Part A*, 2008, **84A**(4), 885–898.
21 M. R. Janes and D. A. Fruman, Immune Regulation by Rapamycin: Moving Beyond T Cells, *Sci. Signaling*, 2009, **2**(67), pe25.
22 E. Pape, M. Parent, A. Pinzano, A. Sapin-Minet, C. Henrionnet and P. Gillet, *et al.*, Rapamycin-loaded Poly(lactic-*co*-glycolic) acid nanoparticles: preparation, characterization, and in vitro toxicity study for potential intra-articular injection, *Int. J. Pharm.*, 2021, **609**, 121198.
23 J. Li, S. G. Kim and J. Blenis, Rapamycin: One Drug, Many Effects, *Cell Metab.*, 2014, **19**(3), 373–379.
24 S. C. Johnson and M. Kaeberlein, Rapamycin in aging and disease: maximizing efficacy while minimizing side effects, *Oncotarget*, 2016, **7**(29), 44876–44878.
25 J. Gallo, N. Vasimalai, M. T. Fernandez-Arguelles and M. Bañobre-López, Green synthesis of multimodal 'OFF–ON' activatable MRI/optical probes, *Dalton Trans.*, 2016, **45**(44), 17672–17680.
26 B. Issa, I. M. Obaidat, B. A. Albiss and Y. Haik, Magnetic nanoparticles: surface effects and properties related to biomedicine applications, *Int. J. Mol. Sci.*, 2013, **14**, 21266–21305.
27 L. García-Hevia, M. Bañobre-Lopez and J. Gallo, Recent progress on manganese-based nanostructures as responsive MRI contrast agents, *Chem. – Eur. J.*, 2018, **24**(2), 2–13.
28 Y. Dessie, S. Tadesse, R. Eswaramoorthy and B. Abebe, Recent developments in manganese oxide based nanomaterials with oxygen reduction reaction functionalities for energy conversion and storage applications: a review, *J. Sci.: Adv. Mater. Devices*, 2019, **4**(3), 353–369.
29 A. K. Gupta and M. Gupta, Synthesis and surface engineering of iron oxide nanoparticles for biomedical applications, *Biomaterials*, 2005, **26**(18), 3995–4021.
30 C. Vieira Rocha, V. Gonçalves, M. C. da Silva, M. Bañobre-López and J. Gallo, PLGA-Based Composites for Various Biomedical Applications, *Int. J. Mol. Sci.*, 2022, **23**(4), 2034.
31 K. Patel, C. Atkinson, D. Tran and S. N. Nadig, Nanotechnological Approaches to Immunosuppression and Tolerance Induction, *Curr. Transp. Rep.*, 2017, **4**(2), 159–168.
32 R. de Almeida R, J. Gallo, A. C. C. da Silva, A. K. O. da Silva, O. D. L. Pessoa and T. G. Araújo, *et al.*, Preliminary Evaluation of Novel Triglyceride-Based Nanocomposites for Biomedical Applications, *J. Braz. Chem. Soc.*, 2017, **28**(8), 1547–1556.
33 J. Gallo, I. S. Alam, I. Lavdas, M. Wylezinska-Arridge, E. O. Aboagye and N. J. Long, RGD-targeted MnO nanoparticles as T_1 contrast agents for cancer imaging – the effect of PEG length in vivo, *J. Mater. Chem. B*, 2014, **2**(7), 868–876.
34 Y. Zhang, M. García-Gabilondo, A. Rosell and A. Roig, MRI/Photoluminescence Dual-Modal Imaging Magnetic PLGA Nanocapsules for Theranostics, *Pharmaceutics*, 2020, **12**(1), 1–16.
35 H. U. Liqiang, C. N. Iu, G. Z. Eng, X. W. Ang and D. H. Uang, Determination of Dissolved Oxygen in Water Based on Its Quenching Effect on the Fluorescent Intensity of Complex, *Anal. Sci.*, 2011, **27**(1), 1121–1125.

36 J. Schindelin, I. Arganda-Carreras, E. Frise, V. Kaynig, M. Longair and T. Pietzsch, *et al.*, Fiji: an open-source platform for biological-image analysis, *Nat. Methods*, 2012, **9**(7), 676–682.

37 F. Danhier, E. Ansorena, J. M. Silva, R. Coco, A. Le Breton and V. Préat, PLGA-based nanoparticles: an overview of biomedical applications, *J. Controlled Release*, 2012, **161**(2), 505–522.

38 M. Bañobre-Lopez, L. Garcia-Hevia, F. Cerqueira, F. Rivadulla and J. Gallo, Tunable performance of manganese oxide nanostructures as MRI contrast agents, *Chem. – Eur. J.*, 2018, **24**(6), 1295.

39 N. Jiang, Z. Zhou, W. Xiong, J. Chen, J. Shen and R. Li, *et al.*, Tumor microenvironment triggered local oxygen generation and photosensitizer release from manganese dioxide mineralized albumin-ICG nanocomplex to amplify photodynamic immunotherapy efficacy, *Chin. Chem. Lett.*, 2021, **32**(12), 3948–3953.

40 J. Gallo, B. I. Harriss, J. Hernández-Gil, M. Bañobre-López and N. J. Long, Probing T_1–T_2 interactions and their imaging implications through a thermally responsive nanoprobe, *Nanoscale*, 2017, **9**(31), 11318–11326.

41 N. A. Keasberry, M. Bañobre-López, C. Wood, J. Stasiuk Graeme, J. Gallo and J. Long Nicholas, Tuning the relaxation rates of dual-mode T_1/T_2 nanoparticle contrast agents: a study into the ideal system, *Nanoscale*, 2015, **7**(38), 16119–16128.

42 M. Rohrer, H. Bauer, J. Mintorovitch, M. Requardt and H. J. Weinmann, Comparison of magnetic properties of MRI contrast media solutions at different magnetic field strengths, *Invest. Radiol.*, 2005, **40**(11), 715–724.

43 A. Rónavári, A. Ochirkhuyag, N. Igaz, B. Szerencsés, G. Ballai and I. Huliák, *et al.*, Preparation, characterization and in vitro evaluation of the antimicrobial and antitumor activity of MnO_x nanoparticles, *Colloids Surf., A*, 2024, **688**, 133528.

44 P. Chen, M. Totten, Z. Zhang, H. Bucinca, K. Erikson and A. Santamaría, *et al.*, Iron and manganese-related CNS toxicity: mechanisms, diagnosis and treatment, *Expert Rev. Neurother.*, 2019, **19**(3), 243.

45 W. Abdelwahed, G. Degobert, S. Stainmesse and H. Fessi, Freeze-drying of nanoparticles: formulation, process and storage considerations, *Adv. Drug Delivery Rev.*, 2006, **58**(15), 1688–1713.